Water vapor stable isotope memory effects of common tubing materials

Alexandra L. Meyer[1], Lisa R. Welp[1]

[1]Department of Earth, Atmospheric, and Planetary Sciences, Purdue University, West Lafayette, 47907, United States

Correspondence to: almeyer269@gmail.com or lwelp@purdue.edu

30

Abstract. Water molecules in vapor can exchange with water molecules sticking to surfaces of sampling tubing, and exchange rates are unique for each isotopologue and tubing material. Therefore, water molecules on tubing walls take some time to reach isotopic equilibrium with a new vapor isotopic signal. This creates a memory effect observed as attenuation time for signal propagation in continuous laser-based stable water vapor isotope measurement systems. Tubing memory effects in δD and $\delta^{18}O$ measurements can limit the ability to observe fast changes, and because δD and $\delta^{18}O$ memory are not identical, this introduces transient deuterium excess (D-excess, defined as $\delta D - 8* \delta^{18}O$) artifacts in time-varying observations. A comprehensive performance comparison of commonly used tubing material water exchange properties has not been published to our knowledge. We compared how a large isotopic step change propagated through five commonly used tubing materials, PFA, FEP, PTFE, HDPE, and copper, at two different temperatures and an air flow rate of 0.635 L min^{-1} through approximately 100 feet (~30.5 m) of ¼ in. (6.35 mm) outer diameter (OD) tubing. All tubing materials performed similarly to each other in terms of attenuation times, reaching 95 % completion in less than 45 seconds in all but 2 experiments with slight variations based on temperature. Bev-A-Line XX was also tested, unheated, but it did not reach isotopic equilibrium after an hour, and we cannot recommend its use in water vapor applications. While shorter tubing length and smaller inner diameters shortens the delay of signal propagation through the tubing, they don't greatly change the shape of the attenuation curve or the delay-adjusted attenuation times under these conditions. Our results show that these commonly-used plastic tubing materials are not inferior to copper in terms of isotopic memory under these conditions, and they are easier to work with and are less expensive than copper. Our experience and results from other published studies indicate that maximizing air flow rates through the analyzer is the most effective way to minimize memory effects when accurate high-frequency D-excess measurements are desired.

1 Introduction

In situ laser absorption spectroscopy of water vapor isotopologues has risen in use over the last two decades enabling fast, continuous isotopic measurements (Webster and Heymsfield, 2003; Lee et al., 2005; Griffith et al., 2006; Kerstel et al., 2006). All experimental setups inherently attenuate signal variability due to mixing in the analyzer optical cavities and molecular water interactions with surfaces inside the inlet and analyzer system, especially when different H_2O_v concentrations lead to wetting and drying of the tubing walls. The timescale for signal attenuation can vary greatly based on a wide range of tubing materials, air flow rates, temperatures, and pressures used (Sturm and Knohl, 2010; Griffis et al., 2010; Schmidt et al., 2010; Tremoy et al., 2011; Aemisegger et al., 2012; Galewsky et al., 2016). As condensation in tubing is a concern due to liquid-vapor fractionation, many installations heat the tubing above ambient temperature, use a critical orifice at the tubing inlet to drop pressure in the lines, or do both in order to keep the vapor in the tubing above the dew point (e.g. Griffis et al. 2010; Luo et al. 2019).

Initially, a plastic coated aluminum Synflex tubing (also known as Dekabon or Dekoron) commonly used in the carbon dioxide and water eddy covariance flux community was used in water vapor isotope experiments (Lee et al., 2005; Gupta et al., 2009; Tremoy et al., 2011), but it was found to greatly attenuate the water isotopic signals (Sturm and Knohl, 2010; Griffis et al., 2010; Schmidt et al., 2010; Tremoy et al., 2011). Testing in various labs has led to

the adoption of plastic or metal tubing, but the details of the experiments and results are sparse (Sturm and Knohl, 2010; Griffis et al., 2010; Schmidt et al., 2010; Tremoy et al., 2011; Steen-Larsen et al., 2014). Commonly used tubing material types now include copper (Steen-Larsen et al., 2014) and several types of plastic including polytetrafluoroethylene (PTFE, commonly referred to as Teflon) (Sturm and Knohl, 2010; Griffis et al., 2010),

75   perfluoroalkoxy (PFA) (Schmidt et al., 2010; Tremoy et al., 2011), fluorinated ethylene propylene (FEP) (Luo et al., 2019), and high-density polyethylene (HDPE) (Griffis et al., 2010). Fluorinated polymers (FEP, PFA, and PTFE) are commonly used as transfer lines in chemical, pharmaceutical, food processing, and oil and gas industries because of their chemical- and weather-resistance, as well as their non-stick and dielectric properties (Chemours, 2018). These materials have found favor in water vapor isotope applications for the same reasons.

80   Air tubing choices are important because materials may have different affinities, or degree of attraction, for the isotopologues of water. This affinity causes a delay in the speed at which the isotopologue signals move through the tubing due to exchange rates with water molecules stuck to the walls, called the memory effect. The memory effect is strongest for δD compared to $\delta^{18}O$ due to the stronger hydrogen bonding of the molecules containing deuterium slowing tubing wall exchanges (Sturm and Knohl, 2010; Griffis et al., 2010; Schmidt et al., 2010). This can result in

85   false deuterium-excess (D-excess, defined as $\delta D - 8* \delta^{18}O$) anomalies and is important to minimize when D-excess signals are interpreted as fast temporal-scale atmospheric signals (Managave et al., 2016; Galewsky et al., 2016; Sodemann et al., 2017; Salmon et al., 2019). Memory may be lessened at higher temperatures and faster air flow rates (Griffis et al., 2010; Pagonis et al., 2017).

    It is important to minimize isotopic wall effects in the intake tubing lines and other in-line elements positioned

90   before the analyzer to minimize signal attenuation. Five studies previously reporting memory effects of tubing types tested a maximum of three materials at a time and are summarized in Table 1 (Sturm and Knohl, 2010; Griffis et al., 2010; Schmidt et al., 2010; Tremoy et al., 2011; Steen-Larsen et al., 2014). Most concluded that Dekabon was not suitable for water isotope applications but varied in which tubing was preferred across applications. The National Ecological Observatory Network (NEON) selected FEP for their monitoring installations which has not been widely

95   used in reported studies (Luo et al., 2019). In this study, we tested five of the commonly used and reported best tubing types under nearly identical conditions at two different temperatures to determine which tubing type and temperature combination results in the smallest isotopic signal attenuation. We also tested Bev-A-Line XX, a commonly used tubing material in soil gas studies.

100 **Table 1.** Literature findings

Author, year	Materials Tested	Isotopes Used/Goals	Result
*Schmidt et al. 2010	Stainless steel, PFA, and Dekabon	δD and $\delta^{18}O$, Analyzer calibration	PFA better than SS. Both better than Dekabon.
*Sturm and Knohl 2010	PTFE and Dekabon	δD and $\delta^{18}O$, Analyzer characterization	PTFE better than Dekabon
Griffis et al. 2010	"Natural colored" HDPE, Teflon (PTFE), and Dekabon	δD and $\delta^{18}O$, $\delta^{18}O$ measurements of evapotranspiration in eddy covariance setups	HDPE equal or slightly better than PTFE. Both much better than Dekabon.

| Tremoy et al. 2011 | PFA and Dekabon | δD, δ¹⁸O, and D-excess, Analyzer characterization and D-excess measurements | PFA better than Dekabon |
| *Steen-Larsen et al. 2014 | Copper, stainless steel, and PTFE | δD, δ¹⁸O, and D-excess, environmental controls on D-excess measurements | Copper better than both. |

*Indicates experimental details and results of source-switching experiments are included in the peer-reviewed published materials.

2 Methods

In this study, we tested PFA, FEP, PTFE, HDPE, and copper at ambient and elevated temperatures using self-regulating heat tape. We switched between two isotopically distinct vapor sources to examine memory effects during water vapor stable isotope measurements. We also tested Bev-A-Line XX at ambient temperature.

2.1 Analyzer

A Los Gatos Research, Inc. (LGR) Triple Water Vapor Isotope Analyzer (TWVIA) Off-Axis Integrated-Cavity-Output Spectroscopy system (OA-ICOS) was used for testing. The air flow rate through the analyzer was 0.635 ± 0.006 L min^{-1} run in standard mode at ~40 Torr. The analyzer precision was characterized over 18 hours at approximately 9,300 ppm. The Allan deviation at two seconds for δD and δ¹⁸O was approximately 1.3 ‰ and 0.58 ‰, respectively (Fig. S1, Guerrier et al., 2020). In order to preserve the attenuation curve resolution, no running mean was applied to the δD and δ¹⁸O data. However, a two second averaging interval is the lowest time limit of the Allan deviation code output (Guerrier et al., 2020), so two second averaged Allan deviation values are reported. An Allen deviation plot of analyzer variance (Fig. S1, Guerrier et al., 2020) estimates a two second averaged D-excess precision better than ± 3.3 ‰, and a 10 s average better than ± 1.0 ‰.

2.2 Experimental Setup

The memory effect of the tubing material was tested by switching between two sources of moist air with different isotopic values but nearly identical water vapor mixing ratios (~9,200 ppm, Table S1). A LiCor model LI-610 portable dew point generator (DPG) was used to create a vapor of approximately -187 ‰ δD, -25.6 ‰ δ¹⁸O, and 17.4 ‰ D-excess, measured by the analyzer, from water at 5°C. The second vapor of approximately -31.8 ‰ δD, -5.7 ‰ δ¹⁸O, and 14 ‰ D-excess was produced by a Los Gatos Research Water Vapor Isotope Standard Source (WVISS). DPG-generated vapor isotopic values for the experiments became isotopically enriched over time as water evaporated from the liquid reservoir. Isotopic δD and δ¹⁸O transitions were normalized to a 1 to 0 scale to compare across experiments and adjust for source water and analyzer drift over time. Five replicate switches were completed for each experiment where the vapor sources switched approximately every 64 minutes giving sufficient time to reach a new isotopic equilibrium. We present data through 20 minutes as equilibrium was already established (with the exception of Bev-A-Line XX).

For each experiment, the WVISS programming and internal valve system controlled the switching between the
DPG output connected to the WVISS inlet port and the WVISS (Fig. 1) output to the TWVIA. The WVISS was
connected to the analyzer by approximately 100 foot (~30.5 m, lengths listed in Table S1) long sections of $^1/_4$ in.
(6.35 mm) outer diameter (OD) test tubing for the main experiments. The Swagelok connection to the analyzer
included an extra stainless steel union and ~2.5 in. (~6.4 cm) thick-walled FEP to protect the bulkhead union threads
from wear during the experiment, but this addition is not expected to affect the results significantly. Other tests were
done with a short (62 in. or 1.57 m) and a long (99 feet $^1/_2$ in. or 29.75 m) piece of thick-walled FEP to quantify
sensitivity to tubing length and inner volume. Tubing inner diameters (ID, summarized in Table S1) were $^3/_{16}$ in.
(~4.76 mm) with the exception of HDPE and thick-walled FEP, which were $^1/_8$ in. (~3.18 mm) ID. The thin-walled
FEP tubing was pieced together using three stainless steel Swagelok unions, but this is not expected to affect the
results significantly.

Tubing and self-regulating heat tape (EASYHEAT ADKS-0500, 100 foot (~30.5 m) roof and gutter de-icing kit)
were wrapped in either flexible foam tape (HDPE, PTFE, thick-walled FEP; AP/Armaflex TAP 18230 insulation
tape) or rigid foam pipe insulation (copper, thin-walled FEP, PFA; Tundra brand $^1/_2$ in. or 1.27 cm wall). The
thermocouple probe was placed inside the insulation on the side of the tubing opposite of the heat tape, about three
inches (~7.6 cm) from the end closest to the analyzer inlet. A datalogger recorded the average temperature over the
~10 hour experiments. During heated tubing tests, the tubing was allowed to warm up at least an hour prior to
measurements to let the tubing moisture equilibrate to the elevated temperature and minimize the effects of
degassing water molecules adhered to the tubing from previous experiments. Differences in the insulation properties
of the two materials used and likely differences in thermocouple placement relative to unavoidable gradients in
temperature resulted in differences in average temperatures for each experiment, ranging from 48.6 to 75.2 °C
(Table S1). All heated experiments (average 60 ± 8 °C) are significantly warmer than ambient temperature
experiments (average 24 ± 1 °C).

An external pump (KNF pump, model N920-2.08) was added to the TWVIA to maximize the turnover rate of air
inside the analyzer. The TWVIA itself regulates the outflow to maintain a constant internal pressure, resulting in
discontinuous (jumpy) flow rates which averaged 0.635 ± 0.006 L min^{-1}. This air flow rate led to an analyzer mean
residence time (referred to as residence time) of 3.97 s. Temperature adjusted tubing residence times were 1.0 ± 0.09
s for short thick-walled FEP, 19.7 ± 1.6 s for long thick-walled tubing, and 45.2 ± 2.5 s for long thin-walled tubing.
The test tubing was placed between the WVISS and the TWVIA. Switching between constant isotopic sources,
WVISS and DPG, was controlled by the LGR software and valves inside the WVISS unit. Air flow rates through the
tested tubing were controlled by the TWVIA itself, making the tubing flow rate as slow as possible and the analyzer
flow rate as fast as possible with this set of equipment. The DPG was operated in a continuous fashion, constantly
generating humid air. To maintain these constant conditions, a vent was added before the DPG outlet to the WVISS
inlet to provide an overflow when the WVISS was pushing its humid air stream to the TWVIA. A Dwyer rotameter
(model number VFB-65-SSV) was used to monitor outflow from the vent. This vent air flow rate is not critical to
the tubing tests because it's simply the overflow. An Omega mass flow meter (MFM, 0–30 L min^{-1} range, model
FMA1826A) was used to monitor air flow rates downstream of the TWVIA to verify analyzer conditions remained

unchanged during the experiments. A Mesa Labs Bios Definer 220 primary flow calibrator (Mesa Labs, Lakewood, CO, 50–5,000 sccm, accuracy $\pm$ 1 % of reading) was used to validate the air flow rate through the TWVIA and test tubing at the inlet of the TWVIA prior to the experiments but was not included during the actual experiments. When the primary flow calibrator was removed, no change in the TWVIA outlet flow was detected on the MFM. Rotameter flow rates were verified at the beginning of the experiments using the primary flow calibrator. The DPG vent flow rate was ~0.9 L min^{-1} when the DPG was sampled by the TWVIA and ~1.5 L min^{-1} when the WVISS was sampled.
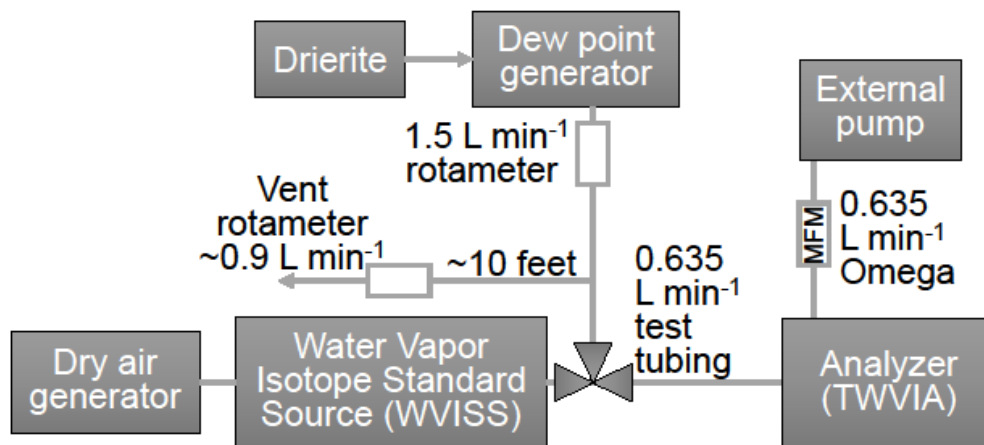
Figure 1. Instrument setup for memory effect tests. The WVISS controls switching between WVISS air and dew point generator air (depicted here as an external 3-way valve, but it's internal to the WVISS), which is passed through test tubing of up to 100 ft and either heated or unheated to the analyzer. The flow through the test tubing is controlled by the analyzer.

2.3 Data Processing

Isotopic values were measured at 1 Hz. No calibration to assign values to the international scale was performed on the isotopic measurements because the transitions were normalized to their starting and ending equilibrium values, resulting in signal transitions from 0 to 1. Isotopic measurements by this analyzer are known to vary with water mixing ratio and potentially drift over long periods of time. Keeping water mixing ratios nearly constant eliminated the need to perform water mixing ratio corrections. Likewise, normalizing the measurements between sources as described below removed any potential influence of instrument or source drift over periods of more than 20 minutes.

For δD and $\delta^{18}O$, the individual transitions from WVISS-to-DPG (DPG-to-WVISS) were normalized from 1 to 0 (0 to 1) and then 5 replicates were averaged to characterize the transition memory. Initial δ values were the average of 5 seconds on either side of the maximum (minimum) value during the lag interval before the signal transition reaches the analyzer. Final δ values were the average of measurements 600–1200 seconds after the source switch. In the experiment with short thick-walled FEP the maximum (minimum) δ value was used due to the speed of the signal transition (i.e. no 10 s average was used). D-excess was calculated as $\delta D - 8* \delta^{18}O$. D-excess was not normalized in the same way as δD and $\delta^{18}O$ because the shape of the attenuation curve is different. A 10 s running

mean was applied, and the 5 replicates were averaged. Replicates were screened based on successful WVISS-to-DPG and DPG-to-WVISS switching and consistent water vapor mixing ratios ensuring that vapor source generators were operating properly. Only one replicate was discarded from the heated PFA experiment due to water mixing ratio variability from the WVISS. We calculated the average D-excess value over 600–1200 seconds after the source switch and subtracted that value from all data points to adjust for small changes in D-excess source waters between replicates, especially in the DPG vapor which undergoes evaporative enrichment. The 600–1200 seconds after the source switch visually appear to be conditions of tubing equilibration and were used to calculate source vapor sample averages given in Table S1 and summarized in Sect. 2.2.

When comparing experiments between different tubing lengths and IDs, differences in the internal volume result in different tubing residence times due to advection. The flow in all experiments was laminar with Reynold's numbers calculated between 579 and 870. In Sect. 3.1 we describe how the experiments are delay-adjusted to compare transitions directly.

Memory analysis included both directions of the isotopic switch. Isotopically enriched-to-depleted (WVISS-to-DPG) figures are presented in the main body of the text, and isotopically depleted-to-enriched (DPG-to-WVISS) transitions are available in the supplemental information (Fig. S3 and S4). While Aemisegger et al. (2012) found the enriched-to-depleted switch exhibited longer attenuation times, this was likely due to the change in water vapor mixing ratio of the sources in their experiment which did not occur here.

2.4 Memory Quantification

Memory effects are analogous to a low-pass filter (e.g. Zannoni et al., 2022). Previous studies have approximated the smoothing of a step-change input as an exponential transition and report a threshold time to some percentage of completion like an e-folding (63 %), 90 %, or 95 % (Sturm and Knohl, 2010; Schmidt et al., 2010; Aemisegger et al., 2012; Steen-Larsen et al., 2014). In some cases, the threshold metrics were obtained from the data directly (Sturm and Knohl, 2010; Steen-Larsen et al., 2014) and in others it appears an exponential function was fit to the data first and the metrics were extracted from the fit (Schmidt et al., 2010; Aemisegger et al., 2012). A second method used in the literature takes the first derivative of the normalized transition (Steen-Larsen et al., 2014) and characterizes an impulse response function using curve fitting (Jones et al., 2017; Kahle et al., 2018). We have quantified memory effect metrics using both methods.

2.4.1 Threshold metrics

We extracted attenuation threshold metrics directly from the normalized and replicate-averaged data (not an exponential fit). An e-folding time corresponds to $\tau = 1/e$ of the signal transition remaining to reach a new value. In this study, we have chosen to estimate attenuation threshold times at 1τ (~63 %) and 3τ (~95 %) completion of the switch to the next δD and $\delta^{18}O$ value, denoted as $t_{63\%}$ or $t_{95\%}$ respectively (Schmidt et al., 2010). These t values are the time the averaged curve intersects the threshold percent value. We chose not to fit exponential curves to extract an e-folding time, because the measured attenuation curves were not accurately described by an exponential curve (not shown). The 1 standard deviation envelope was calculated by taking the standard deviation of the 5 replicates at

each time step. Errors associated with attenuation threshold times were determined by finding the time that the 1 standard deviation envelope of the averaged replicates intersects the completion threshold.

D-excess signals of the source transitions are not unidirectional and memory must be quantified differently. Previous studies reported that δD signals take longer to equilibrate with the surface of tubing materials compared to $\delta^{18}O$ signals due to isotopic effects of hydrogen binding with the tubing walls (Sturm and Knohl, 2010; Griffis et al., 2010; Schmidt et al., 2010; Aemisegger et al., 2012). The D-substituted hydrogen-bonds exchange with the vapor more slowly. This difference leads to a D-excess transition that has a transient anomaly until the δD signal propagation catches up to the $\delta^{18}O$ signal. The direction of the D-excess transient peak depends on the direction of the isotopic signal switch. In the enriched-to-depleted transition, the enriched δD signal is retained on the tubing walls creating a transient, positive anomaly in D-excess while approaching equilibrium. However, in a depleted-to-enriched transition, the depleted δD signal has been preserved on the tubing walls creating a negative D-excess anomaly during isotopic equilibration. The absolute value of the maximum transient peak was identified and associated errors are given as the standard deviation of the time of the maximum peak (Table S2). The threshold chosen to measure completion in D-excess transitions is a 3 ‰ threshold within the new equilibrium value ($t_{3‰}$), determined by the average over 600–1200 s. This threshold is a conservative estimate of analyzer precision of D-excess measurements if δD precision was 1.0 ‰ and $\delta^{18}O$ precision was 0.25 ‰.

To compare the attenuation threshold times across experiments, we adjusted for differences in signal propagation due to the time it takes air to move through the tubing from the WVISS and mixing inside the analyzer, controlled by the air flow rate through the instrument, optical cavity size, test tubing volume, and air flow rate (Schmidt et al., 2010), as well as temperature. Smaller tubing IDs, increased temperature, faster tubing and analyzer air flow rates, and shorter tubing lengths will all shorten lag times associated with a measurement. Lag times were calculated via breakpoint analysis to determine the point where slope changes. We created a linear model using the first 300 s (30 s for short thick-walled FEP tests) of data after the source switched, then utilized the "segmented" function in R's "segmented" package on the time series (Muggeo, 2022). The breakpoint lag estimates likely have an error of a few seconds. The exact uncertainty was not quantified. Average lag times for 100 foot (~30.5 m) thin-walled tubing were 53 s, and 1.5 s for the short thick-walled tubing. In the results, the time axis in the plots were adjusted by fitted location time, and quantitative threshold metrics ($t_{63\%}$ or $t_{95\%}$) in the tables were adjusted by predicted residence time, as discussed in Sect. 3.1.

2.4.2 Impulse response method

In the impulse response method, we take advantage of the first derivative of the observed attenuation curves to clearly identify the timing and rates of change. To decrease the noise in the first derivative, it's necessary to reduce noise in the observed attenuation curves. In previous studies, noise reduction is achieved by fitting a smooth transfer function to the observations. Jones et al. (2017) and Kahle et al. (2018), used a lognormal times lognormal (log-log) function to fit the data, while in Steen-Larsen et al. (2014) only one lognormal is used. For our attenuation curves, neither a single or double lognormal fit the observed data well. Our data was most accurately recreated by a transfer

function of the form in Eq. (1) (with the exception of the depleted-to-enriched transition for HDPE where an additional normal fit was added):

265

$$\delta_{transfer}(t) = c_1 * \left[1 + erf\left(\frac{log(t) - \mu_1}{\sigma_1\sqrt{2}}\right)\right] * \left[1 + erf\left(\frac{log(t) - \mu_2}{\sigma_2\sqrt{2}}\right)\right] * \left[1 + erf\left(\frac{t - \mu_3}{\sigma_3\sqrt{2}}\right)\right] + c_2 \qquad (1)$$

where t is time since switching, σ is the location of each log/normal, μ is the standard deviation of each log/normal, and c_1 and c_2 are scaling factors. The values of $\sigma_1, \sigma_2, \sigma_3, \mu_1, \mu_2,$ and μ_3 are optimized by minimizing the squares of errors using the "DEoptim" global optimization function in the R package of the same name (Ardia et al., 2022).

270 The form of the fitting model here is not that important as long as the observations are faithfully reproduced in the smooth curve fit, as seen in Fig. 2a.

Once a transfer function is fit, the first derivative of the transfer function is calculated to obtain the impulse function. We fit the impulse function by the model in Eq. (2) based on a skew-normal function added to a normal gaussian function.

275

$$\delta_{impulse}(t) = \left(c_1 * \left[\left(\frac{1}{\sqrt{2\pi}}\right) * e^{\frac{-x_1^2}{2}}\right] * \left[\frac{1}{2} + erf\left(\frac{x_1 * \alpha}{\sqrt{2}}\right)\right]\right) + \left(\left[\left(\frac{1}{\sqrt{2\pi}}\right) * e^{\frac{-x_2^2}{2}}\right] * c_2\right) \qquad (2.1)$$

$$x_1 = \frac{(t - \xi)}{\omega} \qquad (2.2)$$

$$x_2 = \frac{(t - \mu)}{\sigma_m} \qquad (2.3)$$

where in the skew-normal terms, ξ is the location of the maximum impulse peak, α is shape, and ω is scale, t is time

280 since switching, σ_m is the standard deviation of the additional PDF and μ is its mean, and c_1 and c_2 are scaling factors. The parameters are solved for using a two-step method: first using the "DEoptim" function (Ardia et al., 2022) to provide an approximate initial guess, and second utilizing the "nls" non-linear least squares function in the "stats" R package of base R (R Core Team, 2023) to provide parameter fine-tuning and uncertainty estimates of each parameter.

285 While Jones et al. (2017) was able to fit impulse functions of their data solely with a skew-normal PDF fit (a standard normal probability distribution function times a standard normal cumulative distribution function, or PDF * CDF), we most accurately reproduced the first derivative by adding an extra PDF in Eq. (2). Figure 2b shows a comparison of the Jones et al. (2017) impulse function skew-normal fit compared to the impulse function fit we used in this study. Our impulse function model fits the memory tail in our experiments better than the skew-normal PDF

290 model from Jones et al. (2017).
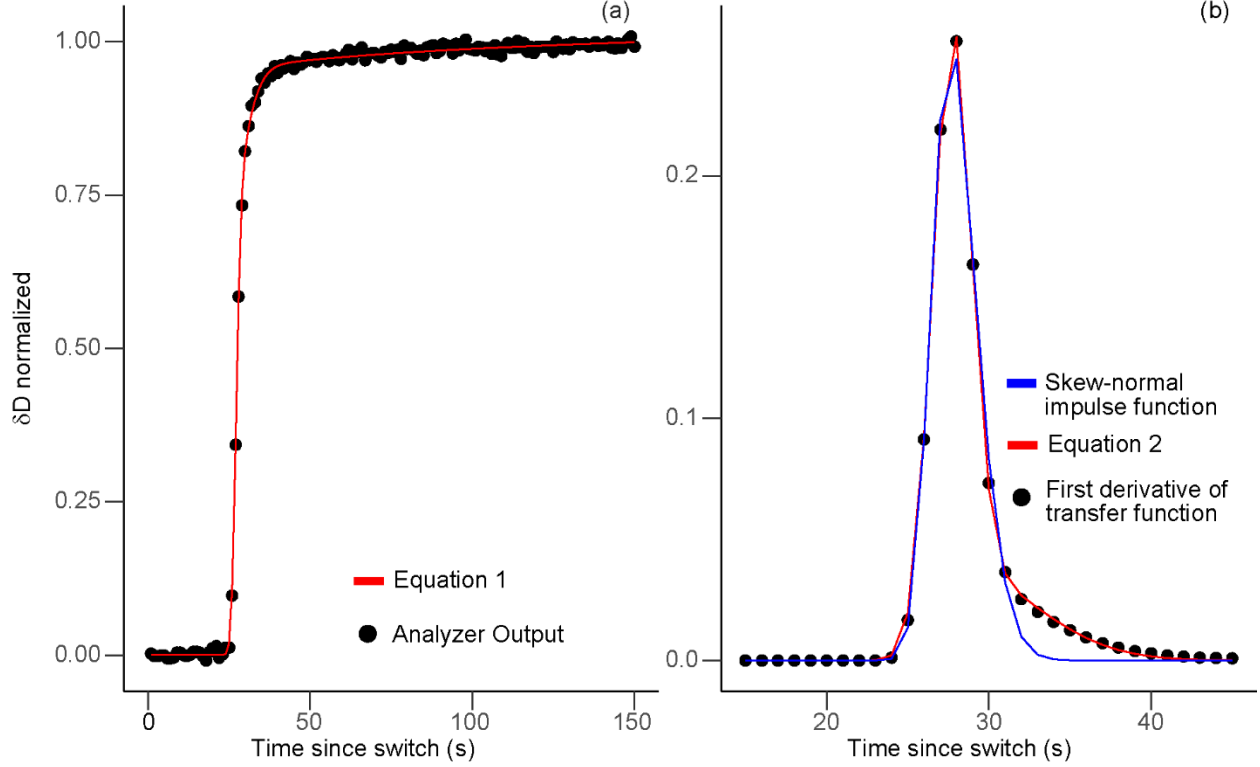
Figure 2. Example of model function fits for the unheated long thick-walled FEP experiment. Panel (a) compares normalized and averaged analyzer output (black dots) with the transfer function given in Eq. (1) (red line). Panel (b) compares the impulse function derived from the first derivative of the transfer function fit evaluated every second (black dots), with the fit from Eq. (2) (red line) and the skew-normal impulse function (blue line) used in Jones et al. (2017) and Kahle et al. (2018).

We extracted two memory metrics from the impulse fitting. First, the skew-normal parameters of shape (α, a descriptor of the shape of the curve or other asymmetry of the distribution) and scale (ω, a measure of the spread of the distribution) were used to estimate a mixing time (σ_s) from Eq. (3). This metric has also been called mixing length in Jones et al. (2017) or diffusive length in Kahle et al. (2018) where analysis time relates distance in the ice cores. The σ_s is a metric of how much mixing occurs due to diffusive flow within the tubing. Error for σ_s is propagated from the errors associated with shape and scale. Second, we also estimate the standard deviation of the additional PDF (σ_m) in Eq. (2) critical for fitting the memory tail in the observations which gives additional information about memory not captured by the skew-normal curve.

$$\beta = \frac{\alpha}{\sqrt{1+\alpha^2}} \qquad (3.1)$$

$$\sigma_s^2 = \omega^2 * (1 - \frac{2\beta^2}{\pi}) \qquad (3.2)$$

$$\sigma_s = \sqrt{\sigma_s^2} \qquad (3.3)$$

3 Results

3.1 Comparison of residence, lag, and location times

The residence time of air in the system is mathematically predicted using the tubing ID, length, temperature, pressure within the tubing, and air flow rate through the tubing (Table S2). Residence times are decreased by decreasing the tubing length and inner diameter or increasing temperature and air flow rates through tubing and analyzer. Average lag times from breakpoint analysis correlate well with predicted residence times (Fig. S2a). For the long thick-walled tubing, the calculated residence time is approximately 19.7 ± 1.6 s, with slight variations due to temperature and small length differences which agrees well with observed lag of 23.1 ± 1.2 s. For long thin-walled tubing, the residence time is approximately 45.2 ± 2.5 s, and average lag time is 53.0 ± 4.0 s. The largest discrepancies between residence and lag times (< 12.5 s) are found in unheated copper and unheated PFA. For short thick-walled FEP, the residence time is 1.0 ± 0.09 s and average lag time is 1.5 ± 1.7 s. Overall, heated tubing lag and residence times were shorter than their unheated counterparts (Table S2).

Similarly, the location time parameter fitted using the impulse response method is the timing of the maximum peak of the impulse function (or the steepest portion of the attenuation curve, discussed in Sect. 2.4.2). The location time is sensitive to the advection lag and the steepness of the isotopic transition. Our estimated location time for the long thick-walled tubing (25.6 ± 1.3 s, Table S2) matches the lag time above when accounting for the < 5 seconds between the initial signal change and the maximum slope of the attenuation curve (or peak in the impulse function). Because of this relationship, location times correlated well with the observed lag times (Fig. S2b) and residence times and are nearly identical to the unadjusted $t_{63\%}$ estimates from the experiments as well (Fig. S2c). The differences in location time between different tubing experiments is not fully explained by differences in residence time predictions. The location time extracted from the δD impulse function is slightly longer than the location time extracted from the $\delta^{18}O$ impulse function, but they correlate well. Heated experiments consistently showed a similar or shorter unadjusted $t_{63\%}$ time in δD and $\delta^{18}O$ compared to their unheated counterparts (Fig. S2d). We suspect this is due to an increased speed of initial signal transition, as the elevated temperature has driven off some water molecules and there is less time required for full equilibration.

To more readily identify differences in curve shape, we adjusted the attenuation curves to a common starting point by subtracting the fitted location time. This is similar to adjusting to lag time (e.g. Steen-Larsen et al., 2014) or predicted residence times. Given uncertainties in the breakpoint analysis of lag time and tubing temperatures which influence residence time, we decided the location time was the most accurate way to collapse the experiments on top of each other in the figures.

3.2 Visual inspection

The mean attenuation curves for the enriched-to-depleted transitions for all experiments (except short and long thick-walled FEP) are compared in Fig. 3 and the depleted-to-enriched results are in Fig. S3. Figures have been adjusted by the $\delta^{18}O$ location time metric in order to more easily compare memory tails of the attenuation curves.

Therefore 0 s in these figures indicates the time of most rapid change in the transfer function and the peak of the impulse function. The δD signal was also $\delta^{18}O$ location adjusted to highlight potential differences between the two isotopologues. Bev-A-Line XX stands out as the tubing material with the longest memory (Fig. 3 and S3). When normalized to start and end at "true" values assigned from a short thick-walled FEP test that occurred immediately

350   prior, the Bev-A-Line XX never reached the 'true' value in either direction of the switch (Fig. 3 and S3). There are slight variations within the rest of the tubing material type and temperature performances. Specifically, thin-walled FEP δD results show slower transitions compared to other tubing experiments. However, this separation is due to a larger location time difference between δD and $\delta^{18}O$ for thin-walled FEP than the rest of the tubings. When adjusted for location, heated experiments often appear to have a less steep δD slope and intercept the $t_{63\%}$ metric later than

355   unheated experiments. We see this specifically in the δD signal for all tubings in the enriched-to-depleted direction with the exception of long thin-walled FEP, and for copper and HDPE in the depleted-to-enriched direction. Location adjusted attenuation curve slopes for $\delta^{18}O$ intercept the $t_{63\%}$ metric later and are shallower for the heated experiments for PFA in the enriched-to-depleted direction and PTFE and copper in the depleted-to-enriched direction (Fig. 3 and S3).

360   δD attenuation times were slower compared to $\delta^{18}O$. Figures 3 and S3 panels b and d also show the mean attenuation curves for the other isotopologue for direct comparison (orange curves). In the enriched-to-depleted transition, propagation of the depleted δD signal was delayed relative to the depleted $\delta^{18}O$ signal (as shown by the orange lines in Fig. 3 and S3 panels b and d), creating a transient positive anomaly in D-excess before equilibrating with the new vapor source isotopic values. D-excess attenuation times are typically much longer than the $t_{95\%}$ times

365   for δD or $\delta^{18}O$ (Table S2). Given differences in D-excess values between sources, we caution overinterpreting the maximum D-excess anomalies between experiments, as evidenced by the different starting points in Fig. 3e.
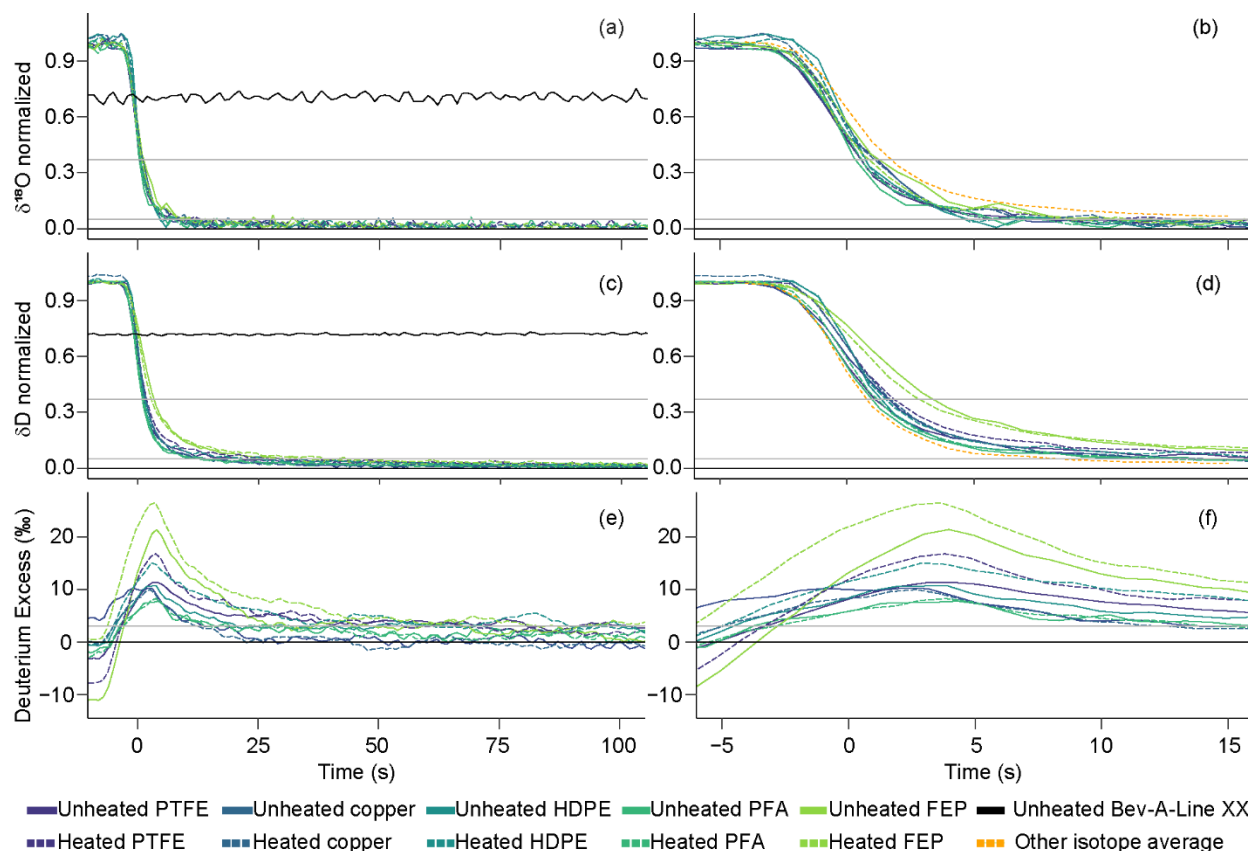
Figure 3. Mean attenuation curves for enriched-to-depleted (WVISS-to-DPG) transitions of five replicates of each tubing type for $\delta^{18}O$ (a, b), δD (c, d), and D-excess (e, f) plotted as location-adjusted time since source switch. The first column (panels a, c, and e) depict time from -5 to 100 s, while the second column (panels b, d, and f) depicts time from -5 to 15 s. Solid lines indicate unheated experiments, while dashed lines indicate heated experiments. An orange curve in panel b shows mean δD for comparison and in panel d shows $\delta^{18}O$ for comparison. To compensate for small differences in isotopic values between experiments, δD and $\delta^{18}O$ are normalized from 1–0 with one at equilibrium with the first vapor source and zero at equilibrium with the second vapor source. D-excess is adjusted to end at 0 ‰ for each experiment. Gray horizontal lines indicate thresholds of 95 % and 63 % transition completion for δD and $\delta^{18}O$, and 3 ‰ for D-excess, while a black line indicates 100 % equilibrium completion for all isotopes. Bev-A-Line XX is shown in panels a and c as a black line and never reaches a normalized 0 or 1 when compared to the experiment immediately prior. Depleted-to-enriched results are presented in the supplemental, as there were no consistent and large differences in attenuation curves between source switching directions.

When testing differences in tubing temperature and dimensions using the same material, properties affecting transit time through the tubing, like tubing length, inner diameter, and effective flow velocities, do not appear to greatly influence the shape of the attenuation curve after location adjustment (Fig. 4 and S4). The short and long thick-walled tubing $\delta^{18}O$ and δD signals overlap each other (Fig. 4b and d), while the long thin-walled tubing has a shallower $\delta^{18}O$ slope (Fig. 4b) and a bigger delay between the δD and $\delta^{18}O$ signal transitions (Fig. 4d). Because we've effectively normalized for tubing length, volume, and temperature through the $\delta^{18}O$ location adjustment, any

differences in the attenuation curve steepness could be attributed to vapor-wall interactions that are independent of bulk flow.
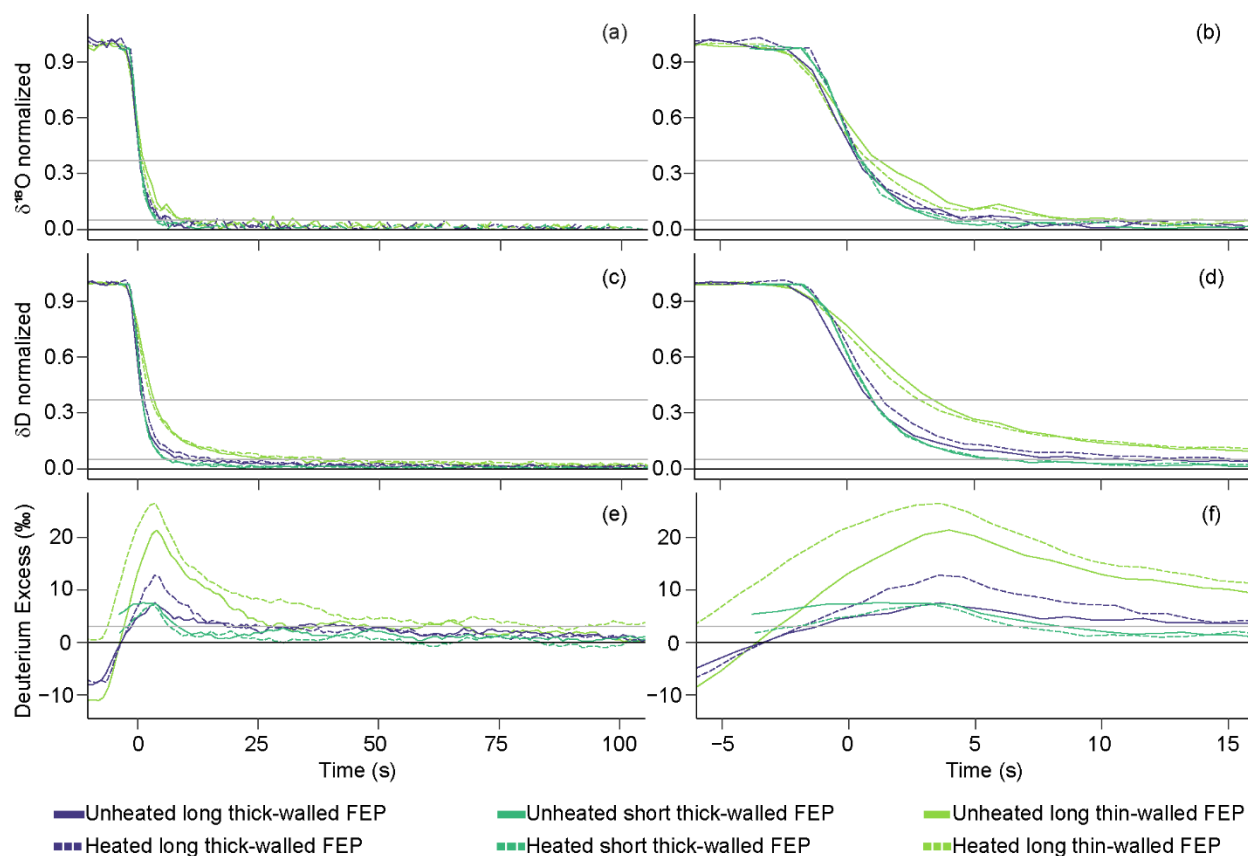
Figure 4. Mean attenuation curves for only FEP tubing for enriched-to-depleted (WVISS-to-DPG) transitions comparing tubing length and inner diameter for $\delta^{18}O$ (a, b), δD (c, d), and D-excess (e, f) plotted as location adjusted time since source switch. The first column (panels a, c, and e) depicts time from -5 to 100 s, while the second column (panels b, d, and f) depicts time from -5 to 15 s. Solid lines indicate unheated experiments, while dashed lines indicate heated experiments. To compensate for small differences in isotopic values between experiments, δD and $\delta^{18}O$ are normalized from 1–0 with one at equilibrium with the first vapor source and zero at equilibrium with the second vapor source, and D-excess is adjusted to end at 0 ‰ for each experiment. Gray horizontal lines indicate thresholds of 95 % and 63 % transition completion for δD and $\delta^{18}O$, and 3 ‰ for D-excess, while a black line indicates 100 % completion for all isotopes. The location adjustment for the short tubing is much shorter than that of the long tubing, leading to a line that appears to start abruptly at ~ -3 s.

3.3 Quantitative memory metrics

Quantitative metrics of σ_s, σ_m, $t_{95\%}$ and $t_{63\%}$ for δD and $\delta^{18}O$, or $t_{3‰}$ and absolute value of the maximum peak for D-excess were also used to compare tubing experiments (Table S2). The different memory metrics calculated provide a

different order of "best" to "worst" tubing materials and conditions based on slight differences, though all tubings appear operationally similar (Table S2). However, some common patterns emerge. According to most impulse response metrics (σ_s and σ_m), short thick-walled FEP has the fastest attenuation impulse response time. The slowest attenuation impulse response time for δD is consistently found in the long thin-walled FEP, while for δ¹⁸O the slowest attenuation impulse response times are found in unheated copper (σ_m, enriched-to-depleted), unheated PFA (σ_s, enriched-to-depleted), and heated PTFE (both metrics, depleted-to-enriched). In terms of residence time adjusted $t_{63\%}$ values, unheated copper is the worst and short thick-walled FEP is the best for both δ¹⁸O and δD. Similarly, δ¹⁸O residence time adjusted $t_{95\%}$ values are longest for unheated copper and shortest for short thick-walled FEP in both directions of the isotopic switch. For residence time adjusted δD $t_{95\%}$ times, long thin-walled FEP is the worst in the enriched-to-depleted direction while heated PTFE is the worst in the depleted-to-enriched direction. Short thick-walled FEP is the best in terms of δD residence time adjusted $t_{95\%}$ time. Short thick-walled FEP was consistently the best for $t_{3‰}$ and the absolute value of the maximum D-excess peak values, while heated long thin-walled FEP was the worse in both metrics in the enriched-to-depleted switch. In the depleted-to-enriched switch direction, heated PTFE was worse for $t_{3‰}$ but for the absolute value of the maximum D-excess peak value, heated long thin-walled FEP was the worst. The rest of the tubing material types vary in their ranking depending on the memory metric used. Overall, heated memory metrics are generally either similar to or faster than those of the unheated memory metrics when comparing the same tubing types (Fig. S1d). However, this pattern does not hold for δD $t_{95\%}$, with differences of up to 15 s between heated and unheated PTFE, with unheated signal equilibrating faster.

Residence time adjusted attenuation threshold times are somewhat consistent with the visual analysis of Fig. 3, 4, S3, and S4. The residence time adjusted $t_{95\%}$ values for δ¹⁸O range from 6.9–22.8 seconds with an uncertainty of up to 24 seconds for individual $t_{95\%}$ values. Measured values of $t_{95\%}$ for δD range from 6.9–48 seconds, with uncertainties of up to 14 seconds. Because of the shallow slope of the attenuation curves at $t_{95\%}$ values contributing to large error estimates, we also report $t_{63\%}$ values because they have smaller uncertainty estimates and may have a different sensitivity to tubing differences. For our analyzer settings, residence time adjusted $t_{63\%}$ values range from approximately 4.9–17.8 s for both δ¹⁸O and δD, with uncertainty on the order of one second. $T_{63\%}$ values are more similar between δ¹⁸O and δD than $t_{95\%}$ values (Fig. S1d). Finally, residence time adjusted $t_{3‰}$ values for D-excess range from 0–93 seconds, while the largest $t_{3‰}$ uncertainty value was 536 seconds. D-excess $t_{3‰}$ values overlap both δD and δ¹⁸O $t_{95\%}$ ranges. We also measured the absolute value of the maximum D-excess peak or the magnitude of the transient anomaly in D-excess signals. These values ranged from ~0–31‰, inclusive of error. The average difference between the beginning and ending D-excess values was 4.0 ‰.

In terms of the impulse response method, σ_m values which characterize the longer memory tail of the impulse function were on average, longer for δD than δ¹⁸O and ranged from 0.66–2.2 ± 0.02 s (Table S2). Mixing times (σ_s) from the skew-normal impulse function fit ranged from 1.4–5.9 ± 1.2 s and were also on average, longer for δD than δ¹⁸O (Table S2). Overall, impulse response metrics varied as expected for δD with length and volume with longer memory times for longer and larger volume tubing, but were inconsistent in δ¹⁸O. We were unable to calculate impulse response metrics for Bev-A-Line XX, as the isotopic switch was not achieved within the hour-long source switching.

3.4 Review of material properties

Predictions of tubing material performance can be made based on material properties. Hydrophobic materials that are nonpolar and have a high relative permittivity (also known as the dielectric constant, or a material's ability to prevent electrical fields from forming) are ideal for water vapor isotope studies as polar water molecules are affected by and can induce electric fields (Aemisegger et al., 2012). As previously shown, δD signal transitions are slowed compared to $\delta^{18}O$ signals, due to isotope-dependent hydrogen-bonding interactions with tubing walls. Limiting these interactions should lead to reduced isotopic attenuation times. Material specifications vary by manufacturer and material purity, but in general, FEP and PTFE materials are expected to have the least amount of water absorption of the tubing types we tested (Table 2). Metals have a relative permittivity value of ~1 due to their sea of electrons, which in this case interact with the polar water molecules. Larger values of relative permittivity are better in this case, as water vapor molecules will be less attracted to the material. HDPE, FEP and PTFE have the highest ability to prevent electrical fields. FEP and PTFE may be expected to have the shortest isotopic attenuation times based on combined water absorption percentage and relative permittivity. However, at the air flow rate we tested, the memory metrics of FEP and PTFE were not noticeably superior to the other tubing tested.

Table 2. Material properties of tubing type options and their water absorption percentages and relative permittivity values.

Material	Water absorption % by tubing weight	Relative Permittivity (Dielectric constant) @ 1 MHz (ε_r)
FEP	<0.01[1]	2.1[2]
PFA	<0.03[1]	2.05–2.06[2]
PTFE	<0.01[1]	2.0–2.1[2]
HDPE	0.10[1]	2.3–2.4[2]
Copper	N/A	~1

[1] after being submerged for 24 hours (ASTM D570). This metric is solely for plastic materials   [2] (Electrical properties of plastic materials, 2021)

4 Discussion

Previous water vapor isotope studies have tried to identify suitable tubing material to use in sample inlets, and authors found several materials to be acceptable. To our knowledge, these materials had not be rigorously tested for wall adsorption/desorption effects leading to memory artifacts. Theory based on principles of gas chromatography and gas-wall partitioning predicts that the residence time of gases adsorbed on tubing walls is linearly proportional to tubing inner diameter and should decrease at higher temperatures as gas saturation concentration changes (Pagonis et al., 2017). The experiments performed in this study begin to test these predictions for water vapor isotopes.

4.1 Effects of material and temperature

We found δD and δ¹⁸O attenuation curves between tubing materials were slightly different, but operationally similar, at the flow rate, humidity, and temperatures tested (Fig. 3, 4, S3, and S4), with the exception of Bev-A-Line XX. Our results are consistent with Griffis et al.'s (2010) assertion that HDPE is similar to PTFE. Similarly, Aemisegger et al., (2012) found little difference in attenuation times with varying PFA tubing temperatures. We were not able to replicate Steen-Larsen et al.'s (2014) finding that copper was better than PTFE. In our study, tubing materials performed similarly when comparing all memory metrics: σ_s, σ_m, $t_{63\%}$, $t_{95\%}$, $t_{3‰}$, and the absolute value of the maximum D-excess peak. Variations in reported material properties presented in Sect. 3.4 predict only slight differences in gas-wall effects in the commonly used tubing materials but were unable to explain the relative differences in memory metrics measured in these conditions. We believe the differences are too small to accurately measure in this experimental setup, partially based on the additional ~4 s residence time of the analyzer optical cell and internal plumbing.

Warmer temperatures are theoretically predicted to reduce attenuation times (Pagonis et al., 2017) by changing the saturation concentration of gases. The lower molar density of the warmer air means there is a shorter residence time through the tubing, increased molecular movement, faster wall exchanges, and fewer molecules stuck to the tubing walls. We found some evidence of this in comparing location times and σ_m from the impulse function method (Table S2). Location times for heated tubings are always faster than their unheated counterparts, and σ_m values are similar to or shorter for heated tubings in most cases. Calculated residence times and observed lag times were also faster for heated tubings, but to varying degrees depending on the tubing. The heated tubing likely has faster residence, lag, and location times due to the decreased number of molecules in the tubing compared to the unheated experiment and possibly also due to decreased wall effects.

Tubing residence time predictions are up to 12 s shorter than the measured breakpoint lag. Uncertainties in tubing residence time (a few seconds), length (a couple inches), and breakpoint lag (a few seconds) account for some of these differences. Tubing temperature measurements in the heated treatment varied depending on the position of the thermocouple relative to the heat cable. It is expected that the tubing was not at a perfectly uniform temperature, but we note that this heating design is commonly used in field conditions and represents likely inlet conditions. However, the lack of uniform temperature control leads to potential temperature-induced differences that are hard to quantify. This should be considered when comparing residence time adjusted memory metrics between experiments. Differences not attributed to variations in temperature, length, or error in the breakpoint lag may be due to wall effects.

4.2 Effects of tubing inner volume and length

The model in Pagonis et al. (2017) indicates that tubing residence time is expected to scale based on length, but should not affect attenuation times sensitive to wall effects. The difference in length in the thick-walled FEP long and short experiments was a factor of 19 (99 ft/5.2 ft, or 30.2 m/1.6 m) which results in the same factor difference in residence time calculations. The breakpoint lag differences between long and short thick-walled FEP tubing was

505   approximately a factor of 8 times faster in the short tubing experiment. While there are slight differences in these memory metrics, this is likely due to the influence of the analyzer. Because the analyzer optical cavity and inner tubing has a residence time of ~ 4 sec, we are unable to resolve the residence time and memory metrics associated with the short FEP tubing (1.0 ± 0.09 s) only. Even with the large length difference, the shape of the isotopic attenuation curves remained similar after location adjustment which removes the length-based residence time

510   differences (Fig. 4 and S4). Residence time adjusted δD $t_{95\%}$ and $t_{63\%}$ times for long thick-walled FEP tubing were at maximum 3.2x and 1.6x greater than the short, respectively. The mixing time scales (σ_s) and the memory tail metric (σ_m) both showed less than a doubling between short and long tubing. These modest differences in wall-effect memory metrics are not explained by the theory in Pagonis et al. (2017).

     The tubing ID affects the residence, lag, and location times, the surface area to air volume ratios, and the flow

515   velocity past the surface of the tubing interior. Pagonis et al. (2017) predicts the residence time of gas molecules on or in the tubing walls changes linearly with respect to tubing ID when the tubing material does not change. In our experiments, ID increased by a factor of 1.5x between thick- and thin-walled FEP ($^1/_8$ in. or ~3.18 mm ID compared to $^3/_{16}$ in. or ~4.76 mm ID). Separation in Fig. 4c and 4d between thick- and thin-walled FEP is exaggerated by the δ^{18}O location adjustment applied to the δD signal, but thin-walled FEP does have a slightly less steep slope and

520   longer $t_{63\%}$ intercept than the thick-walled tubing. Residence time adjusted memory metrics also show a slight increase with ID increase, with an average 1.9x larger memory metric for δD and 1.66x larger memory metric for δ^{18}O between thin- and thick-walled tubing (Table S2). The long thin-walled FEP consistently showed the slowest δD signal transitions of the tubings tested (Fig. 3, 4, S3, and S4 panels c and d). From the location adjusted comparison of the same material (FEP) with different IDs (Fig. 4, δ^{18}O location adjusted plot), we conclude that a

525   bigger ID causes the slower memory metrics. We also note that PTFE and PFA also had the same $^3/_{16}$ in. (~4.76 mm) ID and those experiments showed a faster attenuation threshold time than FEP (Fig. 3). Therefore, the material differences and tubing ID seem to play a role in our experiment, consistent with theory that tubing ID, material density, and partitioning depth will affect the residence time of chemical compounds on or in a tubing wall (Pagonis et al., 2017).

530   In summary, we found that all tubing dimensions, including ID and length, had some effects on the threshold metrics (Fig. 4 and S4) after removing differences in residence times in signal propagation to the analyzer based on tubing inner volume and the temperature influence on molecular density. While these overall memory metric differences exist, they are small in the materials and dimensions tested, and the operational impact among commonly used ¼ in. (6.35 mm) OD tubing inlets is expected to be limited.

535   **4.3 Relative attenuation time differences between δD and δ^{18}O**

     δD signals have been demonstrated to take longer than δ^{18}O signals to isotopically equilibrate with tubing materials due to isotope-dependent hydrogen-bonding interactions with the tubing walls (Sturm and Knohl, 2010; Griffis et al., 2010; Schmidt et al., 2010). This speed difference has been reported as a ratio of attenuation times between the slower δD signal and the faster δ^{18}O signal, and a large range of ratios have been reported. Published results show

540   1.4–3.5x greater attenuation time for δD signals than δ^{18}O signals depending on tubing air flow rate, tubing type,

and memory metric used (Schmidt et al., 2010; Griffis et al., 2010; Aemisegger et al., 2012; Zannoni et al., 2022). For σ_s we found a 0.7–1.8x greater attenuation time for δD signals than δ^{18}O signals. The σ_s metric is not particularly sensitive to the characteristic long δD memory tail. For σ_m, δD values were 0.9–1.7x longer than δ^{18}O values, which is a metric more sensitive to the characteristic long δD memory tail. Location ratios were very similar at 1.0–1.1x greater for δD signals than δ^{18}O which is understandable because that indicates the time of rapid flushing of the analyzer cavity when the new source vapor reaches the analyzer. For $t_{63\%}$, this ratio ranges from 1.0 –1.2x greater, and for $t_{95\%}$ 1.0–2.7x. The threshold metrics are most similar to the quantification metrics used in earlier studies and our results have similar ranges.

4.5 Fitting attenuation curves

The overall attenuation curves of the tested tubing material types, lengths, and temperature conditions had effectively the same reverse sigmoidal shape after fitted location time adjustment. The slight differences in signal attenuation could be due to errors in normalization and location adjustments between experiments, differences in tubing internal roughness, and analyzer noise. Previous studies approximated the attenuation transfer function as an exponential curve (Sturm and Knohl, 2010; Aemisegger et al., 2012; Schmidt et al., 2010), similar to the exponential decay response that would be expected for the residence time distribution function of a continuously stirred reactor (Toson et al., 2019). We found the exponential function was not a satisfactory fit to our experimental observations. A more appropriate mixing analogy could be the axially dispersed plug flow (ADPF) model (Huang and Seinfeld, 2019), as this better matches the reverse sigmoid curve we observe. In the ADPF model, there is a bulk flow that has a diffusive "head" that diverges forwards and backwards from the bulk flow, leading to the observed smoothing of the output signal of an input step-change. This effectively "smears" the observed isotopic signal. While the shape of this transfer function seems appropriate, the Huang and Seinfeld (2019) model does not consider gas-wall exchange effects. The transfer function model we introduce here fits the observations sufficiently well, but more work is needed to match the formulas with mixing theory.

Likewise, the impulse fitting method we used is more complicated than previously used (Jones et al., 2017; Kahle et al., 2018). We were able to estimate a mixing time metric (σ_s) from the skew-normal and a memory tail metric (σ_m) from our modified impulse function fitting method. We believe these metrics are signals of diffusion mixing and isotopic wall effects. Mathematically describing the influence of isotopic wall effects using a transfer and impulse function is potentially useful for correcting out memory effects in water vapor isotope measurements, as suggested by Massman and Ibrom (2008) and others (e.g. Aemisegger et al., 2012; Steen-Larsen et al., 2014). Similar corrections have been achieved in the ice core and liquid water isotope analysis communities (e.g. Jones et al., 2017; Kahle et al., 2018; Vallet-Coulomb et al., 2021). We found more complicated transfer and impulse function models were necessary to fully capture the memory effects in the vapor inlet system compared to the mostly liquid inlet systems described before (e.g. Jones et al., 2017; Kahle et al., 2018; Vallet-Coulomb et al., 2021). This should provide a starting point for future work removing the low-pass filter effects on continuous water vapor measurements.

5 Implications for measurements

Longer attenuation times smooth signal variability and mask high-frequency features. Therefore, the magnitude and speed of atmospheric signal variability as well as the analyzer and sample intake performance are important considerations when planning for ambient water vapor isotopic measurements. We found very small differences among tubing materials under the experimental conditions tested here. While different analyzer air flow rates are not presented in this study, it is known that analyzer flow rate strongly influences sample residence time in the optical cavity of these analyzers and the speed of signal transitions. The Aemisegger et al., (2012) findings that attenuation times were controlled more by analyzer residence times than PFA intake tubing is supported by the results presented in this study.

Though Bev-A-Line XX was the only material in this study that performed particularly poorly, prior research clearly identified Dekabon tubing as unsuitable (Sturm and Knohl, 2010; Griffis et al., 2010; Schmidt et al., 2010; Tremoy et al., 2011). We also suggest testing the effect of any in-line elements like flow meters, mass flow controllers, or filters on isotopic signal attenuation, especially if they are made from materials not tested in this study. Our experience found a mass flow meter that introduced a large memory effect (not presented here).

5.1 Low atmospheric variability measurements

For stationary measurements with one intake and high air flow rates, tubing selection among commonly used materials is not as much of a concern as air advecting past the intake typically changes slowly compared to tubing attenuation time scales we quantify here. Conroy et al., (2016) for example, observed vapor on Manus Island, Papua New Guinea that changed by 22.3 ‰ in $\delta^{18}O$ and 154.8 ‰ in δD, with the largest change being ~25 ‰ δD over a duration of a few hours. The instant isotopic step change in our experiment (17.6 ‰ in $\delta^{18}O$ and 136 ‰ in δD) is extreme compared to typical atmospheric variability at a stationary inlet. For stationary measurements, any of the tested tubing materials besides Bev-A-Line XX should be suitable and would not be expected to produce large transient D-excess artifacts due to memory differences between δD and $\delta^{18}O$.

5.2 High atmospheric variability measurements

For measurements that need high temporal resolution of small atmospheric isotopic variability like flux gradient and eddy covariance setups or airborne observations, extra precautions should be taken. Griffis et al. (2010) used spectral analysis in their eddy covariance experiments to show that tube memory effects weren't a concern for $\delta^{18}O$ signals at tubing air flow rates of 12 L min^{-1} and analyzer air flow rates of 1.5 L min^{-1}. However, one can't extend that conclusion to slower air flow rates and analyzer residence times should be compared across analyzer types.

Aircraft campaigns are a special concern, as they observe not only at high temporal (and spatial) resolution, but encounter large and rapid isotopic and humidity variability as well. Especially when conducting vertical profiles, isotopic compositions can vary by hundreds of per mil in δD. Salmon et al. (2019) found δD signal values ranging from -400 to -175 ‰ δD within an ~5 minute vertical profile descent between 1200 to 400 m above ground. Similarly, Sodemann et al. (2017) reported flight sections with >200 ‰ δD variations in under 5 minutes. While

610 data was collected at 1 Hz, their reported data is a 15 s average, which allows them a 975 m horizontal and 75 m vertical resolution (Sodemann et al., 2017). However, that best-case estimate is based on the data averaging interval and does not consider signal attenuation due to tubing isotopic memory or mixing in the optical cavity (Sodemann et al., 2017). Additionally, averaging over long time periods may not remove D-excess memory bias depending on patterns of increasing or decreasing delta values. The wetting and drying of the measurement system during flights

615 with large changes in altitude, and therefore atmospheric specific humidity, may also increase isotopic attenuation times but were not quantified here.

In both eddy covariance and aircraft measurement situations, one might consider increasing air flow through the analyzer and intake tubing and shortening the length of tubing from an intake pickoff point to the analyzer in slow analyzer flow setups as has been suggested in previous studies (e.g. Griffis et al., 2010). While high air flow rates

620 can easily be achieved in the air intake main lines in both high-frequency measurement situations, the air flow rate through the analyzer is typically limited by the analyzer design and control software. If tubing or in-line elements like mass flow controllers affect the speed at which the isotopes are transmitted from the intake to the optical cavity, signals are effectively low-pass filtered (Zannoni et al., 2022). Our experiments show shorter memory effects for shorter tubing compared to longer tubing. Therefore, it is also important to minimize the length of tubing from the

625 intake pickoff point to the analyzer to reduce the residence time of air in the low-flow portion of the system. These considerations should also maximize D-excess data resolution.

5.3 Liquid water measurements

Liquid water isotope analysis is also plagued by memory effects when samples are converted to the vapor phase for spectral isotopic analysis, especially in applications measuring samples with large isotopic differences in the same

630 batch. Common protocols recommend multiple replicate injections and discarding the first few to remove carryover from the previous sample (IAEA, 2009; Penna et al., 2012; Coplen and Wassenaar, 2015). In both OA-ICOS and cavity ring-down spectroscopy, Penna et al. (2012) found that when measuring samples with large isotopic differences, up to eight out of eighteen injections had to be ignored to limit memory effects. When analyzing highly depleted Antarctic samples ranging from −231.7 ‰ to −421.1 ‰ for δD, memory effects of up to 14 ‰ were found

635 in the first injection compared to the "true" value. Liquid water analysis is one example of a case where air flow rates and temperatures of transfer lines are fixed by the instrument design. Material properties inside the analyzer are important, but this study finds little difference between commonly used material types. Waiting for equilibrium in the optical cavity may minimize the memory effect, but a time-efficient method to increase sample throughput is to mathematically correct for these repeatable effects rather than attempting to minimize them (e.g. de Graaf et al.,

640 2020; Vallet-Coulomb et al., 2021; Hachgenei et al., 2022). Or, in the case of de Graaf et al., (2020), one can measure small vapor samples on a background of humid air to reduce memory effects. Work is also being done in the ice core community to correct out signal mixing based on transfer function fitting methods (e.g Jones et al., 2017; Kahle et al., 2018). These memory correction approaches may provide examples of methods to reconstruct input signal variability from smoothed continuous vapor isotope measurements as well.

645

6 Conclusions

We tested the water isotopic exchange properties of PFA, FEP, PTFE, HDPE, copper, and Bev-A-Line XX. The commonly used materials tested here perform similarly. It does not seem necessary to standardize materials used to measure stable water vapor isotopologues to make accurate and comparable measurements in most situations, when using analyzers with similar residence times. We cannot recommend Bev-A-Line XX for use in water vapor applications due to extremely long attenuation times. Warmer temperatures did shorten the residence time, lag, and location metrics of the impulse function and $t_{63\%}$ threshold times across all long tubing experiments but results were not always consistent for $t_{95\%}$. While differences may be found among tubing material types at lower humidity or while changing humidity, these experiments are beyond the scope of this study. Larger tubing IDs were predicted to increase memory metrics proportionally based on gas-wall partitioning theory (Pagonis et al., 2017), and we found that tubing ID and length had some effects on the threshold metrics after removing differences in residence times. The experiments here showed overall memory metric differences do exist, but that they are small in the materials and dimensions tested. In experimental settings, operational impact among commonly used ¼ in. (6.35 mm) OD tubing inlets is expected to be limited.

Researchers must understand the limitations of the air flow conditions and wall effects of their instrumental and intake setups to limit signal memory effects, especially if low air flow rates are a constraint or if there are large isotopic variations over short periods of time. Our experience and results from other published studies indicate that maximizing air flow rates through the analyzer is the most effective way to minimize memory effects when accurate high-frequency D-excess measurements are desired. As each individual analyzer is unique, users are advised to test their analyzer for memory effects with no intake tubing. Our results show that these plastic tubing materials are not inferior to copper in terms of isotopic memory under the tested conditions, and they are easier to work with and are less expensive than copper. As with most decisions, environmental conditions, cost, and preference may influence the type of tubing selected.

Code/Data Availability

All figure data and scripts, as well as an example workup code, are available at https://doi.org/10.4231/T6J3-H649 (Meyer and Welp, 2023).

Author Contributions

ALM and LRW designed the experiments and conducted them. ALM adapted code from LRW and added to it for this project, as well as analyzed data. ALM wrote the manuscript draft. ALM and LRW edited the document.

Competing Interests

 The authors declare that they have no conflict of interest.

Acknowledgements

We thank Matthew Binkley (MS Materials Engineering) for valuable discussion of material properties.

Financial Support

AM was supported by a Purdue Doctoral Fellowship and the National Science Foundation Graduate Research Fellowship Program under Grant No. (DGE-1333468). Any opinions, findings, and conclusions or recommendations

expressed in this material are those of the authors and do not necessarily reflect the views of the National Science Foundation.

685 **Review Statement**

We thank the editor Thomas Röckmann and three anonymous referees, as well as community commenter Jonathan Keinan, for their time, suggestions for improvement, and patience.

References

Aemisegger, F., Sturm, P., Graf, P., Sodemann, H., Pfahl, S., Knohl, A., and Wernli, H.: Measuring variations of $\delta^{18}O$ and δ^2H in atmospheric water vapour using two commercial laser-based spectrometers: an instrument characterisation study, Atmos. Meas. Tech., 5, 1491–1511, https://doi.org/10.5194/amt-5-1491-2012, 2012.

Ardia, D., Mullen, K., Peterson, B., Ulrich, J., and Boudt, K.: DEoptim: Global Optimization by Differential Evolution Version 2.2-8, CRAN [code], https://cran.r-project.org/package=DEoptim, 2022.

Chemours: An introduction to Chemours^{TM} fluoropolymers, C–11311., The Chemours Company, FC, LLC, 2018. https://www.chemours.com/en/-/media/files/teflon/intro-to-fluoropolymers.pdf?rev=a43531c7fc5c406d86ced4425f2330b4, last access: 14 July 2022.

Conroy, J. L., Noone, D., Cobb, K. M., Moerman, J. W., and Konecky, B. L.: Paired stable isotopologues in precipitation and vapor: A case study of the amount effect within western tropical Pacific storms, Journal of Geophysical Research: Atmospheres, 121, 3290–3303, https://doi.org/10.1002/2015JD023844, 2016.

Coplen, T. B. and Wassenaar, L. I.: LIMS for Lasers 2015 for achieving long-term accuracy and precision of δ^2H, $\delta^{17}O$, and $\delta^{18}O$ of waters using laser absorption spectrometry, Rapid Communications in Mass Spectrometry, 29, 2122–2130, https://doi.org/10.1002/rcm.7372, 2015.

Galewsky, J., Steen-Larsen, H. C., Field, R. D., Worden, J., Risi, C., and Schneider, M.: Stable isotopes in atmospheric water vapor and applications to the hydrologic cycle, Rev. Geophys., 54, 809–865, https://doi.org/10.1002/2015RG000512, 2016.

de Graaf, S., Vonhof, H. B., Weissbach, T., Wassenburg, J. A., Levy, E. J., Kluge, T., and Haug, G. H.: A comparison of isotope ratio mass spectrometry and cavity ring-down spectroscopy techniques for isotope analysis of fluid inclusion water, Rapid Communications in Mass Spectrometry, 34, e8837, https://doi.org/10.1002/rcm.8837, 2020.

Griffis, T. J., Sargent, S. D., Lee, X., Baker, J. M., Greene, J., Erickson, M., Zhang, X., Billmark, K., Schultz, N., Xiao, W., and Hu, N.: Determining the oxygen isotope composition of evapotranspiration using eddy covariance, Boundary-Layer Meteorol, 137, 307–326, https://doi.org/10.1007/s10546-010-9529-5, 2010.

Griffith, D. W. T., Jamie, I., Esler, M., Wilson, S. R., Parkes, S. D., Waring, C., and Bryant, G. W.: Real-time field measurements of stable isotopes in water and CO_2 by Fourier transform infrared spectrometry, Isotopes in Environmental and Health Studies, 42, 9–20, https://doi.org/10.1080/10256010500503098, 2006.

Guerrier, S., Balamuta, J., Bakalli, G., Molinari, R., Lee, J., Radi, A., Xu, H., Zhang, Y., and Claussen, N.: avar: Allan Variance Version 0.1.1, CRAN [code], https://CRAN.R-project.org/package=avar, 2020.

Gupta, P., Noone, D., Galewsky, J., Sweeney, C., and Vaughn, B. H.: Demonstration of high-precision continuous measurements of water vapor isotopologues in laboratory and remote field deployments using wavelength-scanned cavity ring-down spectroscopy (WS-CRDS) technology, Rapid Communications in Mass Spectrometry, 23, 2534–2542, https://doi.org/10.1002/rcm.4100, 2009.

Huang, Y. and Seinfeld, J. H.: A note on flow behavior in axially-dispersed plug flow reactors with step input of tracer, Atmospheric Environment: X, 1, 100006, https://doi.org/10.1016/j.aeaoa.2019.100006, 2019.

IAEA: Laser spectroscopic analysis of liquid water samples for stable hydrogen and oxygen isotopes, International Atomic Energy Agency, Vienna, Germany, 2009.

Jones, T. R., White, J. W. C., Steig, E. J., Vaughn, B. H., Morris, V., Gkinis, V., Markle, B. R., and Schoenemann, S. W.: Improved methodologies for continuous-flow analysis of stable water isotopes in ice cores, Atmospheric Measurement Techniques, 10, 617–632, https://doi.org/10.5194/amt-10-617-2017, 2017.

730   Kahle, E. C., Holme, C., Jones, T. R., Gkinis, V., and Steig, E. J.: A Generalized Approach to Estimating Diffusion Length of Stable Water Isotopes From Ice-Core Data, Journal of Geophysical Research: Earth Surface, 123, 2377–2391, https://doi.org/10.1029/2018JF004764, 2018.

Kerstel, E. R. T., Iannone, R. Q., Chenevier, M., Kassi, S., Jost, H.-J., and Romanini, D.: A water isotope (^{2}H, ^{17}O, and ^{18}O) spectrometer based on optical feedback cavity-enhanced absorption for in situ airborne applications, Appl.
735   Phys. B, 85, 397–406, https://doi.org/10.1007/s00340-006-2356-1, 2006.

Lee, X., Sargent, S., Smith, R., and Tanner, B.: In situ measurement of the water vapor ^{18}O/^{16}O isotope ratio for atmospheric and ecological applications, J. Atmos. Oceanic Technol., 22, 555–565, https://doi.org/10.1175/JTECH1719.1, 2005.

Luo, H., Pingintha-Durden, N., and Smith, D.: NEON sensor command, control and configuration (C3) document:
740   eddy covariance storage exchange (NEON.DOC.000465) Version F, NEON (National Ecological Observatory Network), 71, 2019.

Managave, S., Jani, R., Narayana Rao, T., Sunilkumar, K., Satheeshkumar, S., and Ramesh, R.: Intra-event isotope and raindrop size data of tropical rain reveal effects concealed by event averaged data, Climate Dynamics, 47, 981–987, https://doi.org/10.1007/s00382-015-2884-7, 2016.

745   Massman, W. J. and Ibrom, A.: Attenuation of concentration fluctuations of water vapor and other trace gases in turbulent tube flow, Atmospheric Chemistry and Physics, 8, 6245–6259, https://doi.org/10.5194/acp-8-6245-2008, 2008.

Meyer, A. and Welp, L. R.: Water vapor stable isotope memory effects of common tubing materials, https://doi.org/10.4231/T6J3-H649, 2023.

750   Muggeo, V. M. R.: segmented: Regression models with break-points / change-points (with possibly random effects) estimation Version 1.6-0, CRAN [code], https://CRAN.R-project.org/package=segmented, 2022.

Pagonis, D., Krechmer, J. E., de Gouw, J., Jimenez, J. L., and Ziemann, P. J.: Effects of gas–wall partitioning in Teflon tubing and instrumentation on time-resolved measurements of gas-phase organic compounds, Atmospheric Measurement Techniques, 10, 4687–4696, https://doi.org/10.5194/amt-10-4687-2017, 2017.

755   Penna, D., Stenni, B., Šanda, M., Wrede, S., Bogaard, T. A., Michelini, M., Fischer, B. M. C., Gobbi, A., Mantese, N., Zuecco, G., Borga, M., Bonazza, M., Sobotková, M., Čejková, B., and Wassenaar, L. I.: Technical Note: Evaluation of between-sample memory effects in the analysis of δ^{2}H and δ^{18}O of water samples measured by laser spectroscopes, Hydrology and Earth System Sciences, 16, 3925–3933, https://doi.org/10.5194/hess-16-3925-2012, 2012.

760   Electrical properties of plastic materials: https://www.professionalplastics.com/professionalplastics/ElectricalPropertiesofPlastics.pdf, last access: 17 December 2021.

R Core Team: R: A Language and Environment for Statistical Computing, http://www.R-project.org/, 2023.

765   Salmon, O. E., Welp, L. R., Baldwin, M. E., Hajny, K. D., Stirm, B. H., and Shepson, P. B.: Vertical profile observations of water vapor deuterium excess in the lower troposphere, Atmospheric Chemistry and Physics, 19, 11525–11543, https://doi.org/10.5194/acp-19-11525-2019, 2019.

Schmidt, M., Maseyk, K., Lett, C., Biron, P., Richard, P., Bariac, T., and Seibt, U.: Concentration effects on laser-based δ^{18}O and δ^{2}H measurements and implications for the calibration of vapour measurements with liquid
770   standards, Rapid Commun. Mass Spectrom., 24, 3553–3561, https://doi.org/10.1002/rcm.4813, 2010.

Sodemann, H., Aemisegger, F., Pfahl, S., Bitter, M., Corsmeier, U., Feuerle, T., Graf, P., Hankers, R., Hsiao, G., Schulz, H., Wieser, A., and Wernli, H.: The stable isotopic composition of water vapour above Corsica during the HyMeX SOP1 campaign: insight into vertical mixing processes from lower-tropospheric survey flights, Atmos. Chem. Phys., 17, 6125–6151, https://doi.org/10.5194/acp-17-6125-2017, 2017.

775   Steen-Larsen, H. C., Sveinbjörnsdottir, A. E., Peters, A. J., Masson-Delmotte, V., Guishard, M. P., Hsiao, G., Jouzel, J., Noone, D., Warren, J. K., and White, J. W. C.: Climatic controls on water vapor deuterium excess in the marine boundary layer of the North Atlantic based on 500 days of in situ, continuous measurements, Atmospheric Chemistry and Physics, 14, 7741–7756, https://doi.org/10.5194/acp-14-7741-2014, 2014.

Sturm, P. and Knohl, A.: Water vapor δ^2H and δ^{18}O measurements using off-axis integrated cavity output
780   spectroscopy, Atmos. Meas. Tech., 3, 67–77, https://doi.org/10.5194/amt-3-67-2010, 2010.

Toson, P., Doshi, P., and Jajcevic, D.: Explicit residence time distribution of a generalised cascade of continuous stirred tank reactors for a description of short recirculation time (bypassing), Processes, 7, 615, https://doi.org/10.3390/pr7090615, 2019.

Tremoy, G., Vimeux, F., Cattani, O., Mayaki, S., Souley, I., and Favreau, G.: Measurements of water vapor isotope
785   ratios with wavelength-scanned cavity ring-down spectroscopy technology: new insights and important caveats for deuterium excess measurements in tropical areas in comparison with isotope-ratio mass spectrometry, Rapid Communications in Mass Spectrometry, 25, 3469–3480, https://doi.org/10.1002/rcm.5252, 2011.

Vallet-Coulomb, C., Couapel, M., and Sonzogni, C.: Improving memory effect correction to achieve high-precision analysis of δ^{17}O, δ^{18}O, δ^2H, ^{17}O-excess and d-excess in water using cavity ring-down laser spectroscopy, Rapid
790   Communications in Mass Spectrometry, 35, e9108, https://doi.org/10.1002/rcm.9108, 2021.

Webster, C. R. and Heymsfield, A. J.: Water isotope ratios D/H, ^{18}O/^{16}O, ^{17}O/^{16}O in and out of clouds map dehydration pathways, Science, 302, 1742–1745, https://doi.org/10.1126/science.1089496, 2003.

Zannoni, D., Steen-Larsen, H. C., Peters, A. J., Wahl, S., Sodemann, H., and Sveinbjörnsdóttir, A. E.: Non-equilibrium fractionation factors for D/H and ^{18}O/^{16}O during oceanic evaporation in the north-west Atlantic region,
795   Journal of Geophysical Research: Atmospheres, 127, e2022JD037076, https://doi.org/10.1029/2022JD037076, 2022.